ELSEVIER

Nuclear Engineering and Design 146 (1994) 337–348

Nuclear Engineering and Design

Modeling supersonic flows through a gas-continuous two-fluid medium

James C. Liu, Philip Colella †, Per F. Peterson, Virgil E. Schrock

Department of Nuclear Engineering and †Department of Mechanical Engineering, University of California, Berkeley, CA 94720, USA

Abstract

This paper presents the application of a numerical method for gas dynamics to model supersonic flows in a gas continuous, two-fluid medium. Specifically, flows in the two-phase medium are modeled only as single-phase compressible flow in a fixed, complex, multidimensional geometry. Coupling effects involving liquid response to interfacial forces are neglected. The motivation for development stems from the desire to predict blast interaction with liquid blankets in Inertial Confinement Fusion reactors. The model uses a second-order extension of Godunov's finite difference method to solve Euler's time-dependent equations of gas dynamics. The method uses a uniform Cartesian grid and a simple method for treating complex boundary geometries. The algorithm uses operator splitting to solve gas dynamics in multiple dimensions. Results of several problems are qualitatively and quantitatively compared with previous work and experimental data.

1. Introduction

Over the last several years, Inertial Confinement Fusion (ICF) has been gaining more attention as a viable future power source. As a result, increased effort has been focused on analyzing the hydrodynamic phenomena which follow after the fusion energy release. One such phenomenon under study is that of blast venting though blankets in ICF reactors.

In the ICF concept, lasers or heavy ion beams are used to heat deuterium and tritium containing pellets which are repetitively injected into the vessel. The subsequent fusions release energy in the form of neutrons, X-rays and debris kinetic energy. To shield the first structural wall (FSW) from radiation, most ICF concepts incorporate a blanket made of either liquid lithium or molten Li_2BeF_4 (Flibe). More specifically, the HYLIFE ICF concept [1,2] uses an encircling array of falling slabs or cylindrical jets of lithium or Flibe. Highly energetic vapor or blast material is generated in the central cavity due to x-ray ablation of the exposed blanket surfaces. The blast material must vent quickly through the blanket so as to avoid accelerating the liquid and generating a waterhammer on the FSW. This phenomenon is one of supersonic flow through a gas continuous two-phase medium.

Blast venting through ICF reactor blankets was first studied by Glenn [3] who modeled the problem as supersonic flow through a packed

SSDI 0029-5493(93)E0240-K

columnar array of cylinders. The model that was developed treated the problem as compressible flow through a one-dimensional channel with varying cross-section, and used steady-state drag coefficients. Although radiation heat transfer was considered in the calculation, shock effects and multidimensional effects were not considered.

This paper describes the application of a multi-dimensional numerical method for single-phase gas dynamics in computing transient super sonic flow through a gas continuous two-phase medium, namely, ICF blankets. The model uses a second-order extension of Godunov's finite difference method to solve Euler's time-dependent equations of gas dynamics. A uniform Cartesian grid and a simple method for treating complex boundary geometries in Cartesian coordinates are used, while multi-dimensional capability is achieved through operator splitting. The technique has been incorporated into a code called the Transient Shockwave Upwind Numerical Analysis Method for ICF (TSUNAMI), which can be adapted to compute gas dynamics for general problems of super sonic gas flows through complex geometries where the gas is the continuous phase.

2. Modeling and assumptions

The model assumes that extremely rapid gas flows through coarsely dispersed liquid, as considered in ICF environments, can be approximated as single-phase gas dynamics flows through a fixed geometry, i.e., objects in the flow field remain rigid and stationary during venting. The accuracy of this assumption depends on constraints such as inertia possessed by the objects, surface pressure history, and the duration of venting. For most of the time domain considered in this study, which is on the order of several hundred microseconds to one millisecond, scaling as well as pressure histories from preliminary computations indicate only a small change in geometry. Liquid deformation, acceleration and droplet stripping at high Weber and Bond numbers on liquid surfaces were not considered.

Other simplifying assumptions are the vapor behaves as an inviscid, ideal gas with constant specific heat ratio and no heat transfer from the gas to the liquid is allowed. This last assumption greatly simplifies the computation, and because energy loss through heat and mass transfer out of the vapor is prohibited, it provides conservatism in estimating impulsive surface forces that are then used in separate calculations to estimate the work done in accelerating the liquid jets or slabs of the blanket material.

The problem of supersonic flow is posed in the context of numerically solving Euler's equations of inviscid compressible flow. In two Cartesian space variables, the conservative form of the equation is:

$$\frac{\partial U}{\partial t} + \frac{\partial F^x}{\partial x} + \frac{\partial F^y}{\partial y} = 0, \tag{1}$$

where

$$U = (\rho, \rho u, \rho v, \rho E)^{\mathrm{T}}, \tag{1a}$$

$$F^x = (\rho u, p + \rho u^2, \rho uv, \rho uE + up)^{\mathrm{T}}, \tag{1b}$$

$$F^y = (\rho v, \rho uv, p + \rho v^2, \rho vE + vp)^{\mathrm{T}}, \tag{1c}$$

$$E = e + (u^2 + v^2)/2, \tag{1d}$$

$$e = \frac{p}{\rho(\gamma - 1)}. \tag{1e}$$

U is the vector of conserved quantities, F the flux tensor, ρ, density, u, x-velocity, v, y-velocity, p, pressure, and e, internal energy.

3. Numerical algorithm

The numerical algorithm used here is an explicit, upwind, conservative, finite difference scheme based on a second-order extension developed by Colella [4] of Godunov's [5] first-order method. The goal of Godunov's method is to compute the flux F of mass, momentum, and energy – Eqs. (1b) and (1c) – across cell edges for a given time step, and then to perform differencing to find the value of U, Eq. (1a), at the new time. It is assumed that the density, velocity and pressure for the entire flow field are initially known.

The Godunov method treats the jump in properties at each cell edge as a discontinuity and solves for the flux F using the characteristic solution to the generalized one-dimensional Riemann shock problem. The method presented here uses a uniform Eulerian grid in Cartesian coordinates. The scheme is first developed in one-dimension, then standard operator splitting (Leveque [6], Strang [11]) is used to extend the algorithm to two dimensions. This paper only outlines the method and does not include derivations, which may be found in the referenced articles [4,5]. The method has 4 steps.

Step (1) involves discretizing the initial data for the uniform Cartesian grid and assigning distinct average values of density, velocity and energy to each cell (Fig. 1).

Step (2) involves estimating to second order accuracy the conserved quantities on either side of every cell boundary at the half time step. This is also known as constructing the time-centered left and right states which become the inputs to the Riemann problem at the cell edges. Characteristics and flux-limiting are used to determine the average properties at the half-time step. The notation used here for time-centered values may appear implicit. This however, is only notation. The method presented here is entirely explicit. For left and right states at the cell edge between cells i and $i+1$, the solution developed by Colella [4] is:

$$V_{i+1/2,\mathrm{L}}^{n+1/2},\ V_{i+1/2,\mathrm{R}}^{n+1/2}\quad \left[V=(\rho,u,p)^{\mathrm{T}}\right], \tag{2}$$

$$\rho_{(i+1/2,\mathrm{L})}^{n+1/2}=\left(\tilde{\rho}_{\mathrm{L}}^{-1}-\beta_{\mathrm{L}}^{0}-\beta_{\mathrm{L}}^{-}\right)^{-1}, \tag{2a}$$

$$u_{(i+1/2,\mathrm{L})}^{n+1/2}=\tilde{u}_{\mathrm{L}}-\beta_{\mathrm{C}}^{-}C_i, \tag{2b}$$

$$p_{(i+1/2,\mathrm{L})}^{n+1/2}=\tilde{p}_{\mathrm{L}}+\beta_{\mathrm{L}}^{-}C_i^2, \tag{2c}$$

$$\rho_{(i+1/2,\mathrm{R})}^{n+1/2}=\left(\tilde{\rho}_{\mathrm{R}}^{-1}-\beta_{\mathrm{R}}^{0}-\beta_{\mathrm{R}}^{+}\right)^{-1}, \tag{2d}$$

$$u_{(i+1/2,\mathrm{R})}^{n+1/2}=\tilde{u}_{\mathrm{R}}+\beta_{\mathrm{R}}^{+}C_{i+1}, \tag{2e}$$

$$p_{(i+1/2,\mathrm{R})}^{n+1/2}=\tilde{p}_{\mathrm{R}}+\beta_{\mathrm{R}}^{+}C_{i+1}^2, \tag{2f}$$

where flux limiting is achieved by:

$$\beta_{\mathrm{L}}^{-}=-\left(\Delta u_i-\frac{\Delta p_i}{C_i}\right)\frac{\Delta t}{2\rho_i^n\Delta x_i}\qquad \text{if } \lambda_i^{-}>0,$$

$$=0\qquad \text{otherwise;} \tag{3a}$$

$$\beta_{\mathrm{R}}^{+}=-\left(\Delta u_{i+1}-\frac{\Delta p_{i+1}}{C_{i+1}}\right)\frac{\Delta t}{2\rho_{i+1}^n\Delta x_{i+1}}\qquad \text{if } \lambda_{i+1}^{+}<0,$$

$$=0\qquad \text{otherwise;} \tag{3b}$$

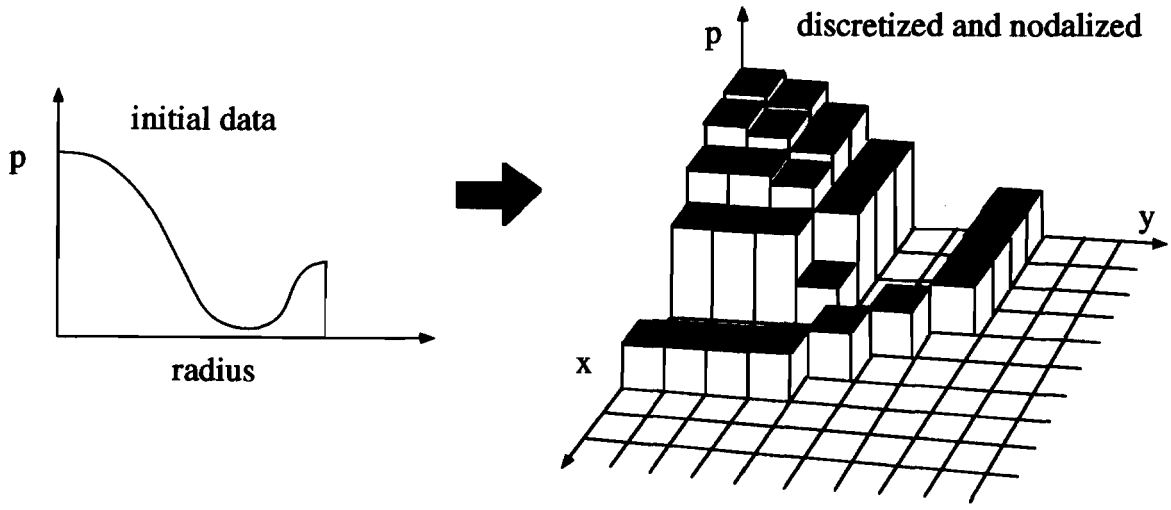

Fig. 1. Example of taking initial pressure data and assigning average values to corresponding cells.

$$\beta_L^0 = -\left(\frac{\Delta p_i}{C_i^2} - \frac{\Delta \rho_i}{\tilde{\rho}_L \rho_L^0}\right) c_i \frac{\Delta t}{2\Delta x_i} \quad \text{if } \lambda_i^0 > 0,$$
$$= 0 \quad \text{otherwise;} \tag{3c}$$

$$\beta_R^0 = \left(\frac{\Delta p_{i+1}}{C_{i+1}^2} - \frac{\Delta \rho_{i+1}}{\tilde{\rho}_R \rho_R^0}\right) c_{i+1} \frac{\Delta t}{2\Delta x_{i+1}} \quad \text{if } \lambda_{i+1}^0 < 0,$$
$$= 0 \quad \text{otherwise;} \tag{3d}$$

for

$$\tilde{q}_L = q_i^n + \tfrac{1}{2}\left(1 - \frac{\Delta t}{\Delta x_i}(\min(\lambda_i^+, 0))\right)\Delta q_i, \tag{4a}$$

$$\tilde{q}_R = q_{i+1}^n - \tfrac{1}{2}\left(1 + \frac{\Delta t}{\Delta x_{i+1}}(\min(\lambda_{i+1}^-, 0))\right)\Delta q_{i+1}, \tag{4b}$$

$$\tilde{q}_L^0 = q_i^n + \tfrac{1}{2}\left(1 - \frac{\Delta t}{\Delta x_i} u_i\right)\Delta q_i, \tag{4c}$$

$$\tilde{q}_R^0 = q_{i+1}^n - \tfrac{1}{2}\left(1 + \frac{\Delta t}{\Delta x_{i+1}} u_{i+1}\right)\Delta q_{i+1}, \tag{4d}$$

$q = \rho$, u, v, and p;
c = sound speed;
$C = \rho c$, and $\lambda_i^0 = u_i$, $\lambda_i^- = u_i - c_i$, and $\lambda_i^+ = u_i + c_i$.

The Δq's are computed using a second-order upwind difference known as the MUSCL scheme of van Leer [12] and are given by:

$$\Delta q = \min(\tfrac{1}{2}|q_{i+1}^n - q_{i-1}^n|, 2|q_{i+1}^n - q_i^n|,$$
$$2|q_i^n - q_{i-1}^n|) \cdot \text{sign}(q_{i+1}^n - q_{i-1}^n)$$
$$\text{if } (q_{i+1}^n - q_i^n)(q_i^n - q_{i-1}^n) > 0,$$
$$= 0 \quad \text{otherwise.} \tag{5}$$

One observes that computing left and right states for the Riemann problem only requires ρ, u, and p, while computing the left and right $\tilde{q}$'s and Δq's also requires v, the transverse velocity. The reason involves operator splitting. The solution to the one-dimensional Riemann problem only requires density, normal-direction velocity and pressure, but the actual computation of flux, Eq. (1b), for the two-dimensional operator split scheme must also include the correct transverse velocity. This is analogous to curve fitting the one-dimensional solution to account for coupling of the transverse velocity in two dimensions. The method for evaluating transverse velocity is given in Eq. (6).

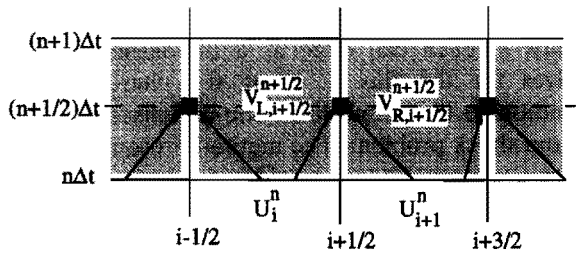

Fig. 2. Schematic representation of computing time-centered left and right states as inputs into the Riemann problem.

Step (3) is finding the solution to the Riemann problem for the given left and right states. This requires an algorithm known as a Riemann solver. The solver computes the solution of characteristics in x/t-space which emerge as a result of the interaction between any arbitrary initial left and right states. For an Eulerian frame calculation with fixed mesh, one chooses the solution in x/t space corresponding to $x/t = 0$. The details are not included in here but are provided in the reference by Colella [4]. The solution to the Riemann problem provides the cell edge values for ρ^*, u^*, and p^* at $(x, t) = (i + 1/2, n + 1/2)$ used in computing the flux $F^x_{i+1/2}$. The flux calculation also requires knowing v, the transverse velocity, which is defined as:

$$v_{i+1/2}^{*n+1/2} = \tilde{v}_L + \beta_L^t \quad \text{if } u^* \geq 0,$$
$$= \tilde{v}_R - \beta_R^t \quad \text{if } u^* < 0, \tag{6}$$

where

$$\beta_L^t = c_i \Delta v_i \frac{\Delta t}{2\Delta x_i} \quad \text{if } u_i^n > 0,$$
$$= 0 \quad \text{otherwise;} \tag{6a}$$

and

$$\beta_R^t = c_{i+1} \Delta v_{i+1} \frac{\Delta t}{2\Delta x_{i+1}} \quad \text{if } u_{i+1}^n < 0,$$
$$= 0 \quad \text{otherwise.} \tag{6b}$$

Step (4) is the conservative differencing of the fluxes to obtain values for density, velocity and energy at the new time. In the x-direction, this is given simply by:

$$U_i^{n+1} = U_i^n + \frac{\Delta t}{\Delta x_i}\left(F^x_{i-1/2} - F^x_{i+1/2}\right). \tag{7}$$

For extension to two dimensions, operator splitting is used. Operator splitting relies on the approximation:

$$\tilde{U}^*_{i,j} = U^n_{i,j} + \frac{\Delta t}{\Delta x_i}\left(F^x_{i-1/2,j} - F^x_{i+1/2,j}\right), \tag{7a}$$

$$U^{n+1}_{i,j} = \tilde{U}^*_{i,j} + \frac{\Delta t}{\Delta y_j}\left(F^y_{i,j-1/2} - F^y_{i,j+1/2}\right). \tag{7b}$$

In other words, for a single time step, a sweep of the entire grid is first done in the x-direction – the fluxes computed and conservatively differences – then a sweep is repeated in the y-direction with u interchanged with v as the transverse velocity. This scheme intuitively neglects any coupled derivative terms, which may create an error that grows with each time step. Fortunately, Strang [11] showed that sweeping first in the x-direction then y-direction for even time steps, and y-direction then x-direction for odd time steps maintains second-order accuracy in space and time provided that the time step is constant for any two consecutive steps.

The time-step is determined by the Courant condition, which for all nodes is:

$$|u-c|\frac{\Delta t}{\Delta x} \le 1, \quad |u+c|\frac{\Delta t}{\Delta x} \le 1,$$

$$|v-c| \le 1, \quad \text{and} \quad |v+c|\frac{\Delta t}{\Delta y} \le 1. \tag{8}$$

4. Boundary conditions

An approximate method of computing boundary conditions was incorporated to take advantage of the uniform Cartesian geometry in setting up arrays of slabs or cylinders. Two types of boundaries – open and impermeable – are modeled. Open boundaries exist where fewer nodes are desired to reduce the computational effort. Inflow or outflow at an open boundary can be set by a forcing function at the boundary, or, if only outflow is desired (i.e. whatever leaves the system never comes back) then the flux at the boundary cell edge can be set equal to $F(U)$ for U inside the boundary cell. That is:

$$F_0^{n+1/2} = F(U_0^n), \tag{9}$$

where

$$U_0^n = U(\rho_0^n, u_0^n, v_0^n, p_0^n). \tag{9a}$$

An impermeable boundary, on the other hand, permits no flux to pass through normal to the surface. To satisfy this condition in Cartesian coordinates requires first, defining the nodes which lie adjacent to boundaries, second, defining a spatial angle for each boundary node, and third, computing the Riemann solution such that the pressure and density correspond to a zero normal flux across the boundary.

The first step, defining boundaries, requires identifying those nodes which lie on or near the actual boundary. This may establish a somewhat jagged boundary and accuracy will depend on the fineness of the mesh. Once the boundary nodes have been identified, the normal angle into the boundary is assigned to the node. In developing TSUNAMI, the reference angle θ is defined as the angle between the positive, x-axis and a normal vector into the boundary (Fig. 3).

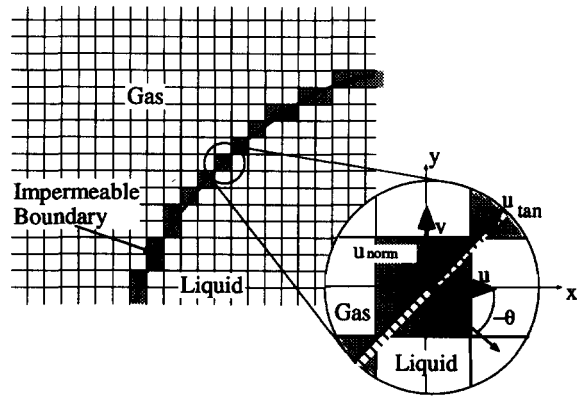

Fig. 3. Schematic representation of grid definition and nodalization of impermeable boundary cells. Shaded cells are boundary cells. Cells on the liquid side are null cells and not subject to computation.

Modeling the zero-normal flux condition at the impermeable boundary employs a technique of mirror imaging. This technique utilizes the Riemann solver to predict the correct density and pressure for a shock or rarefaction contacting an impermeable surface. One begins by creating an imaginary node opposite but directly adjacent to the boundary node, possessing the same density, tangential velocity and pressure, but opposite normal velocity. As with ordinary interior nodes, left and right states must be computed. However, by inspection, one can see that for boundary nodes all the correction terms go to zero, and the result is:

$$\rho_{0,\mathrm{L}}^{n+1/2} = \rho_0^n, \tag{10a}$$

$$u_{n0,\mathrm{L}}^{n+1/2} = u_0^n \cos\theta_0^n + v_0^n \sin\theta_0^n, \tag{10b}$$

$$p_{0,\mathrm{L}}^{n+1/2} = p_0^n, \tag{10c}$$

$$\rho_{0,\mathrm{R}}^{n+1/2} = \rho_0^n, \tag{10d}$$

$$u_{n0,\mathrm{R}}^{n+1/2} = -u_{n0,\mathrm{L}}^{n+1/2}, \tag{10e}$$

$$p_{0,\mathrm{R}}^{n+1/2} = p_0^n. \tag{10f}$$

Equations (10a–f) provide the inputs into the Riemann problem whose solution provides the pressure and density. The tangential velocity at the boundary node:

$$u_{t0}^{n+1/2} = v_0^n \cos\theta_0^n - u_0^n \sin\theta_0^n \tag{11}$$

is decomposed back into x–y coordinates according to:

$$u_0^{*n+1/2} = -u_{t0}^{n+1/2} \sin\theta_0^n, \tag{12a}$$

$$v_0^{*n+1/2} = u_{t0}^{n+1/2} \cos\theta_0^n, \tag{12b}$$

and then all the properties inserted into (1b) or (1c) to compute flux. Conservative differencing is performed using (7a) or (7b). The above technique works because both shock and rarefaction reflections at walls are exactly analogous to the collision of two shocks or rarefactions of equal magnitude.

An important note is that boundary nodes do not necessarily remain boundary nodes when the sweeping directing changes (e.g. a vertical wall appears as a boundary when sweeping in the x-direction but not the y-direction.) Also, the apparent angle of a boundary in one direction changes by $\pi/2$ when sweeping in the other direction.

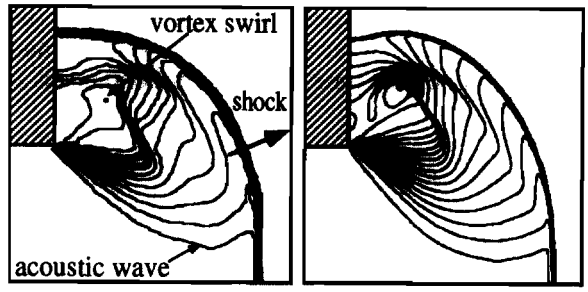

Fig. 4. Iso-density contours of Mach 3 shock in air diffracting around a corner. Left figure computed using TSUNAMI code with 50×50 grid, and right side computed by Carafano [14] as presented by Hillier and Graham [7].

5. Numerical results – benchmarks

The operator split, numerical method used in TSUNAMI, with exception of the current boundary condition method, has been shown to be accurate in computing idealized compressible flow [13,15]. To test the applicability of the approximate boundary conditions, four comparisons are presented here. The first two are qualitative comparisons of shock diffraction around a corner and shock flow past a cylinder while the latter two are quantitative comparisons with experimentally obtained shock retardation and shock venting data. For the first two problems, iso-density contours provide a convenient method of visualizing the gas dynamics and comparing qualitative features. Non-dimensional units are used.

Figure 4 shows a comparison of density contour plots for Mach 3 shocks diffracting around a sharp corner (left TSUNAMI, right Carafano [14]). Some discrepancies exist such as a higher wall shock speed at 90 degrees which results in a flatter and smoother profile than in the other calculation. Also, some of the internal details to the right of the vortex swirl are different. Some of these differences may be attributed to coarser mesh spacing and shorter physical time of calculation in our calculations. Overall, however, most of the major phenomena such as the vortex swirl,

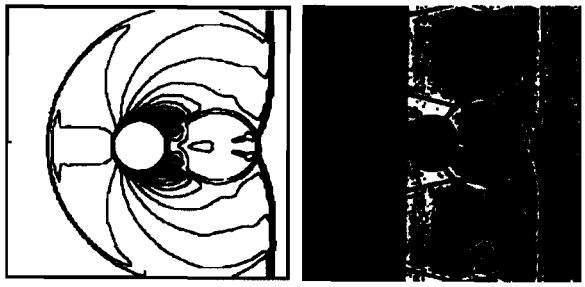

Fig. 5. Comparison of iso-density contours for Mach 1.65 shock in air over a cylinder computed using TSUNAMI with 80×80 grid to Mach 1.65 shock through a bank of cylinders (only one cylinder shown). From Bowman and Niblett [8].

transmitted shock front and downward propagating acoustic wave are all represented.

Figure 5 shows density contours for calculated shock flow over a cylinder compared with a photograph of the real process (Bowman and Niblett [8]). In the calculation, the approximated cylinder is 16 nodes in diameter. Remarkably good agreement exist in the qualitative features between calculation and experiment. However, a small difference does exist in the width and curvature of the Mach stems which trail behind the cylinder. A closer inspection reveals that the cylinder in the photograph is somewhat elliptical, which may be the cause of the discrepancy.

In the third benchmark test, we attempt to predict the shock retardation for the experimental set-up by Kawamura and Kawada [9] shown in Fig. 6, and then compare the computed results with the experimental data. Their use of air at

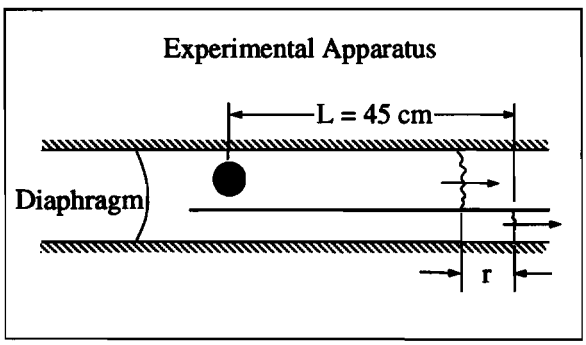

Fig. 6. Experimental apparatus used in experiment to study shock retardation with obstructions in the flow path. From Kawamura and Kawada [9].

Table 1
Shock retardation results

Mach No.	Blockage	Retardation [r/L]	
		Experiment	TSUNAMI
1.25	58%	3.2%	3.1%
	75%	5.4%	6.1%
1.36	58%	3.7%	3.3%
	75%	7.5%	8.0%

approximately standard atmospheric conditions and relatively low supersonic Mach numbers makes the experiment suitable for modeling using idealized compressible flow relations. Table 1 gives a comparison of the results. The calculations are within 5% to 10% of the reported value for shock retardation, and lie well within the reported margins of experimental error. The calculations for 58% blockage tended to under estimate the retardation while the calculations at 78% blockage over estimate the retardation. This was traced back to the nodalization and use of integer spaced grids which resulted in slightly smaller percentage blockage for the 58% case and slightly higher percentage blockage for the 75% case.

The fourth benchmark attempts to predict the pressure transducer profiles for a shock tube experiment, which is used to study shock interactions with an array of vertical, cylindrical liquid jets. The experiment has a square test section with an orifice plate on top and transducers along the side (Fig. 7). Water is delivered down through the orifice plate to establish the jets. A horizontal shock tube then delivers a shock into the test section, which is housed inside a pressure vessel. The ambient gas in the vessel is air. The experiment records the time-dependent pressure on the test section side wall generated when a shock propagates through the jet array. Algorithms were developed to automate the creation of boundary conditions corresponding to the jet array, as were color and grey scale visualization techniques with animation capabilities.

Figure 7 is a computed density grey-scale visualization of shock propagation through the jet array. The first frame shows the shock wave just prior to array contact. The second frame shows

shock venting through the array and also a slightly irregular reflected shock due to the offset in the initial row of jets. The third frame shows venting out the back of the array with preferential venting along the edges of the walls because of the direct line-of-sight. Also, the contact surface between expanding driver gas and the shocked gas now approaches the array and interacts with the reflected shock, causing the reflected shock to reflect again. The last frame shows driver gas stagnating against the first row of jets. The initial shock has already vented through the array and

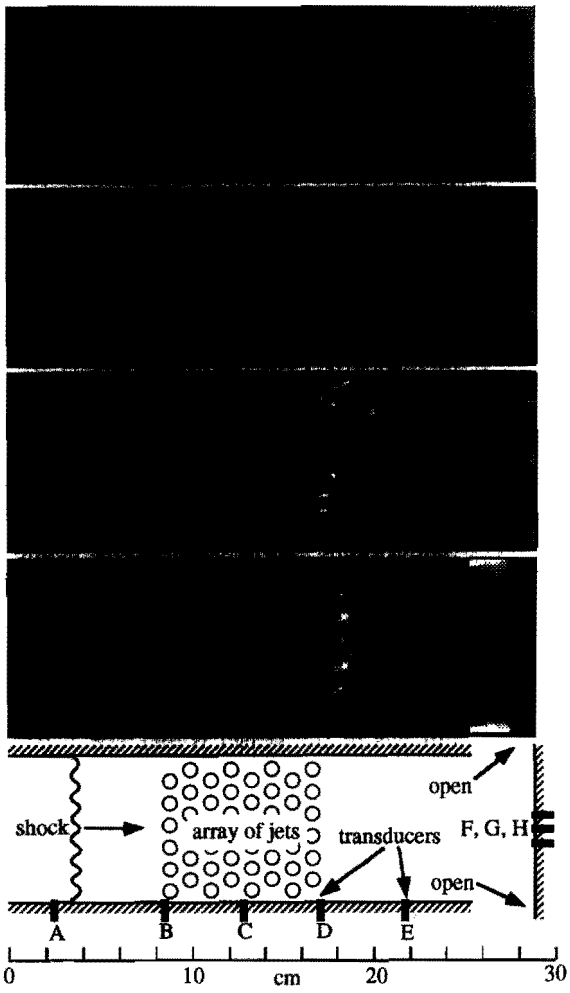

Fig. 7. Computed shock wave interaction with a jet array shown at 75 ms intervals. Grey-scale shows mass density with magnitude increasing from light to dark. A 100×250 grid was used to approximate 48 jet geometry.

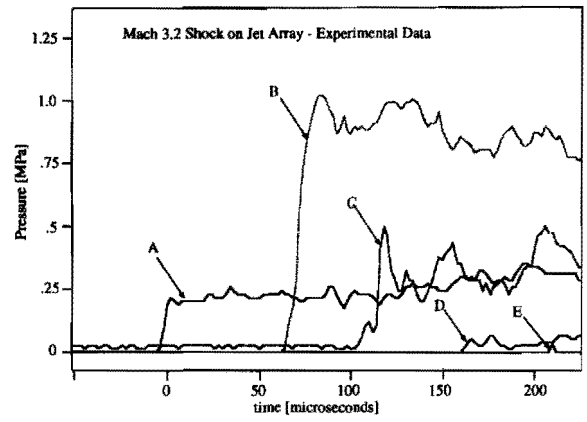

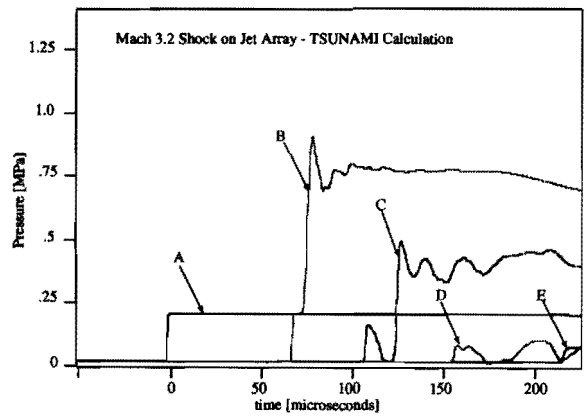

Fig. 8. Two graphs comparing experimental and computed pressure traces for 5 transducers mounted along the side of the test section in the liquid jet array shock tube experiment.

reflected from the back wall with some of the gas escaping through the short open sections on either side at the rear. This generates roll-wave shaped density distributions as flow is redirected and vented out sideways.

Figure 8 is a comparison between experiment and calculation of the transient pressure traces recorded at 5 positions along the wall for a Mach 3.2 shock. The arrival times of the shock as well as the peak pressures compare within 10% for the first 3 traces but show greater error farther downstream where the shock has been attenuated. The greater error downstream is attributable to the difference between the liquid jets in the experiment and solid cylinder approximation in the calculation, and the effect of boundary layers on the test section side walls.

The experimental data shows a number of significant kinks and multiple peaks in the pressure traces arriving at 70, 110, and 160 ms for the second, third, and fourth transducers respectively. The pressure trace at transducer B shows the shock arrival at approximately 70 ms followed by an immediate rise in pressure to nearly 1 MPa. There is however a noticeable change in slope, that is a kink, in the pressure rise near 0.25 MPa. Recalling the location of transducer B from Fig. 7, this corresponds to the initial shock wave reaching transducer B, then striking and reflecting off the first row of jets. There is some small time delay for the reflected overpressure to be

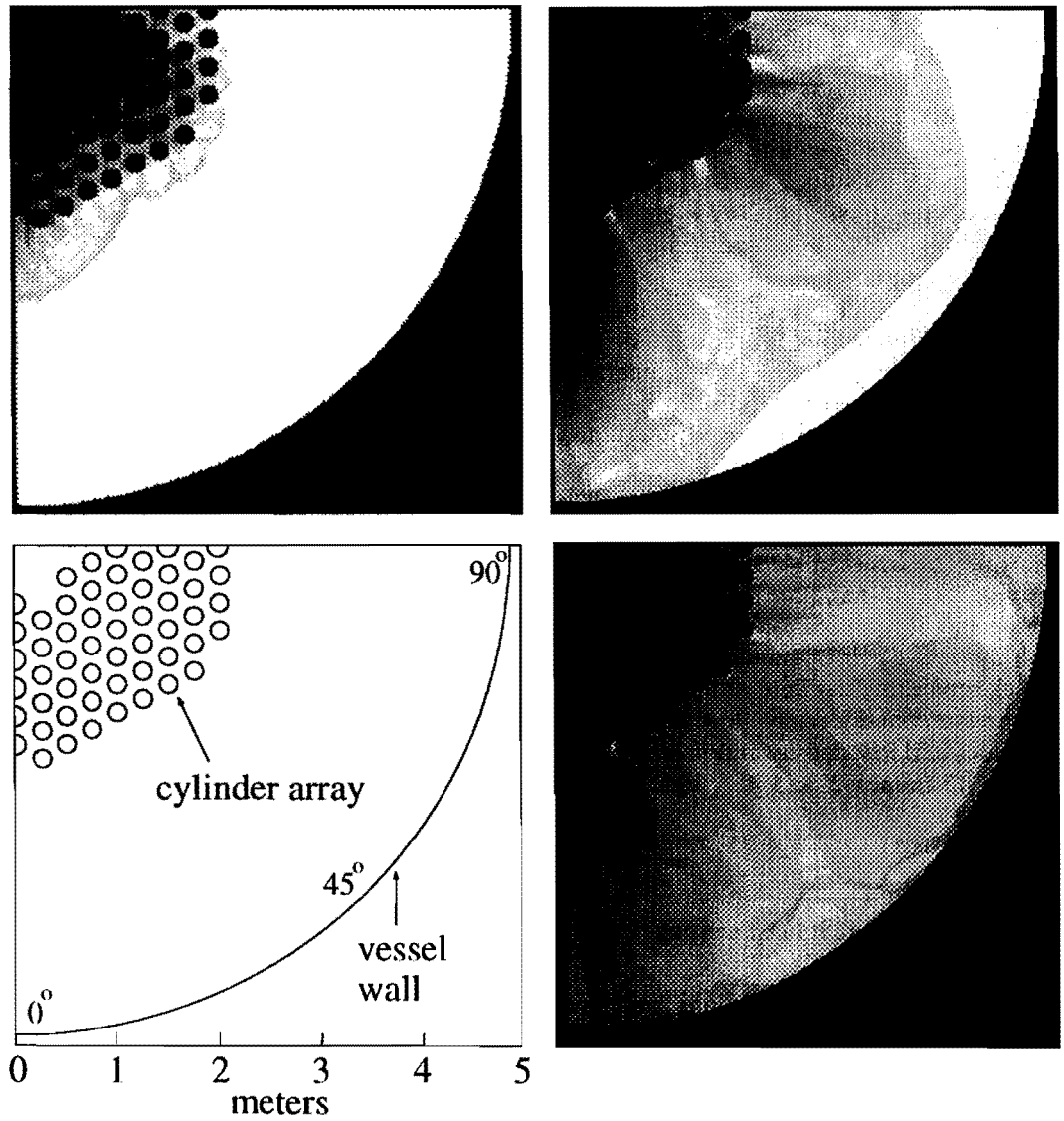

Fig. 9. Computed blast venting through liquid blanket in the HYLIFE-I ICF reactor shown clockwise from top, left at 80 microsecond intervals. Same density grey-scale as in Fig. 6. One-quarter of the reactor cavity is simulated using a 250 × 250 uniform grid with 54 cylindrical jets.

sensed by transducer B. Another interesting phenomenon is the occurrence a pressure spike rising to about 0.12 MPa at transducer C which arrives at 110 ms followed by a larger one rising to 0.5 MPa at 120 ms. The calculation predicts and resolves both the kink in transducer B's pressure trace and the dual peaks in transducer C except with greater time separation. The pressure transducers used in the experiment have a response time of 2 μs. In addition, the shock tube goes through a transition from round to square prior to the test section which can diffuse the shock front. Both of these factors may contribute to a shallower observed pressure rise for the shock. Overall, however, the majority of the venting phenomenon such as shock arrival times, reflected overpressures, and the pressure traces with multiple shock reflections are quantitatively and qualitatively predicted.

Visualization and animation are important techniques in understanding gas dynamics processes. One example is that of supersonic flow separation and its effect on form drag. (One should not confuse this with boundary layer flow separation which is a viscous effect. The gas dynamics here are inviscid.) The code predicts that the surface integrated form drag is greater for the last row of jets than for some interior jets. Visualization reveals that flow is separating over each of the last jets – i.e. each of the last jets almost always has a pair of standing Mach stems off the back separating the field around a jet into a higher pressure and density flow around the front and sides and low density and pressure flow behind (Fig. 7, frames 3 and 4 – light streaks behind last row).

6. Numerical results – ICF blast venting

Two ICF blast venting situations are presented. The first example is a simulation of blast venting through a cylindrical array in the HYLIFE-I ICF reactor [1]. An energy of 2700 MJ has just been released, of which about a third goes into vapor energy. The initial conditions in the central cavity are taken to be the same as in the previous study by Glenn [3], and venting occurs through a 50% packing fraction hexagonal array of 20 cm diameter liquid lithium jets.

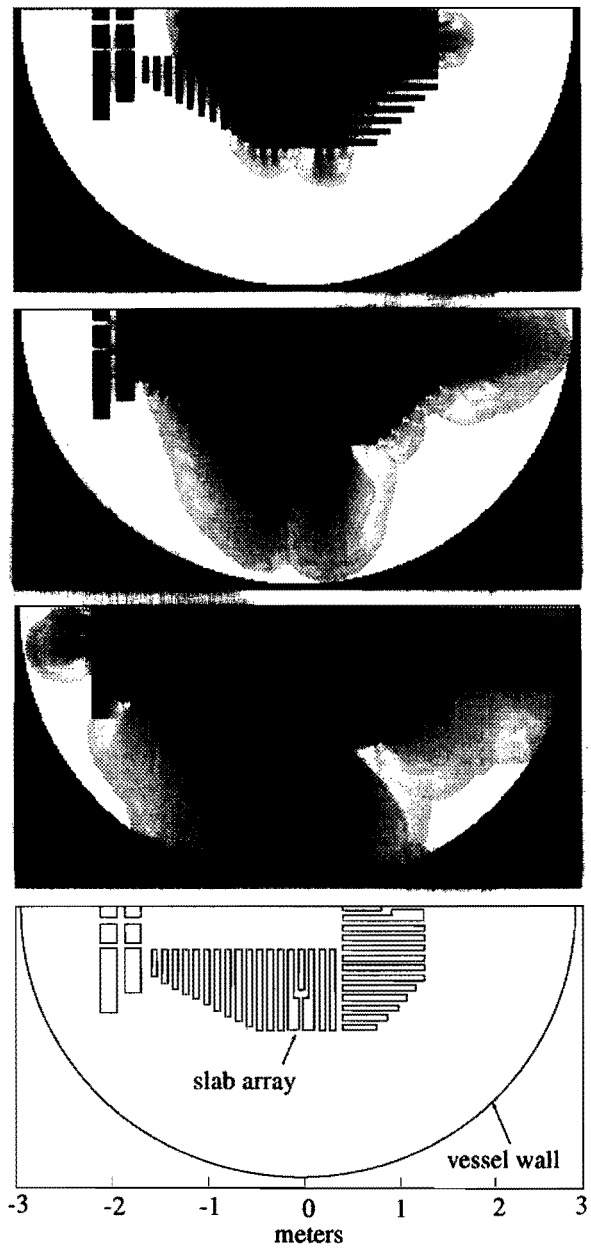

Fig. 10. Computed blast venting through liquid blanket in the HYLIFE-II ICF reactor shown at 90 ms intervals. Same grey scale density as above. One-half of the reactor cavity is simulated using a 300×600 uniform grid with 37 slabs.

The code simulated the first 1000 ms. Figure 9 shows a simulation of blast venting in the HYLIFE-I reactor just described. Blast venting is preferential in the directions with direct line-of-sight out to the vessel wall. Venting in the zero degree azimuthal angle is slightly faster than at the 60 degree position due to the slightly wider spacing in the horizontal direction which is unavoidable in when trying to approximate a hexagonally packed array on an integer Cartesian grid. Flow separation (indicated by light colored zones) is evident behind several outside cylinders for sustained periods of time causing the impulse to these outer jets to be greater than the impulse on jets just inside. This may result in increased FSW erosion due to jet impact.

The code predicts asymmetric wall loading with average wall gas shock pressures over 5 MPa and peak pressures over 35 MPa. Average liquid velocities due to drag are over 200 m/s. These estimates are almost an order of at magnitude larger than previous estimates [3], which did not consider shock or multi-dimensional effects. However, the lack of heat transfer from gas to liquid makes the model conservative. Note that the assumption of stationary geometry does not hold for these high velocities. This indicates that at least for the HYLIFE-I case, it is likely that blanket will close and be propelled destructively toward the FSW.

The second example is blast venting through a complex slab array in the HYLIFE-II [2] reactor cavity. The initial energy release is 350 MJ, a third going into vapor energy. The initial conditions are scaled from the previous HYLIFE study [3] except the working fluid is now Flibe. The code simulates blast venting up to 500 ms. Figure 10 shows the flow visualization for the HYLIFE-II reactor with a 58% packing fraction of liquid slabs. As in Fig. 9, blast venting is preferential in the directions with direct line-of-sight out to the vessel wall. Wall loading is also very asymmetric. The code predicts much more mild average wall gas shock of 1 MPa with peak pressures of around 3 MPa. Average liquid velocity is predicted to be about only 1 m/s. More specific results for blast venting through blankets in ICF can be references in another article by the authors [10].

7. Conclusions

A method of modeling transient, supersonic flows through a gas continuous, two-phase medium by considering only single phase gas dynamics in a fixed, two-dimensional geometry has been presented. The method incorporates a proven second-order Godunov finite difference method with operator splitting to track shocks with high resolution in two dimensions. The use of Cartesian coordinates and straight forward boundary conditions lends this method to many other applications where a need exists for computing gas dynamics in complex geometries. The combined numerical method and boundary conditions have been compared with other numerical and experimental data and have been found to show good qualitative and quantitative agreement.

Application of the code to early time blast venting in the HYLIFE ICF reactor indicate that asymmetric wall loading, FSW erosion, and waterhammer will be important considerations in ICF reactor design.

The present model has been shown to be applicable at early times for gas continuous two-fluid mediums where the gas can be approximated by ideal compressible flow. Future work to enhance the accuracy and applicability to ICF will require consideration of real gases, radiation, condensation, moving boundaries, fluid–structure interactions, and viscous effects.

8. Nomenclature

C Lagrangian (mass coordinate) sound speed,
c sound speed,
E total energy – sum of kinetic and internal,
e specific internal energy,
F tensor representing flux of U,
p pressure,
q generic variable which can be ρ, u, v, or p
U vector of conserved gas dynamics quantities,
u x-direction velocity,
V vector of primitive variables (ρ, u, p),
v y-direction velocity,
x abscissa in Cartesian coordinates,
y ordinate in Cartesian coordinates.

8.1. Greek symbols

β intermediate calculation variable,
γ ratio of specific heats; adiabatic const.,
λ characteristic velocity u, v, $u+c$, $v+c$, $u-c$, or $v-c$,
θ angle made with positive x-axis,
ρ mass density.

8.2. Superscripts

$\sim$ intermediate solution,
$-$ left traveling wave ($u-c$ or $v-c$) solution
$+$ right traveling wave ($u+c$ or $v+c$) solution,
0 zero-wave (density wave, u or v) solution,
n index for time step,
x x-direction (horizontal),
y y-direction (vertical),
$*$ solution at the edge between two nodes,
T matrix or vector transpose.

8.3. Subscripts

0 boundary node,
i generic index in x-direction,
j generic index in y-direction,
n normal direction,
t tangential direction,
L left-hand state,
R right-hand state.

9. Acknowledgment

Work by authors in the Dept. of Nuclear Engineering performed under auspices of the U.S. Department of Energy for the Lawrence Livermore National Laboratory under contract W-7405-Eng-48. Work by author in the Dept. of Mechanical Engineering performed under the auspices of DARPA and the National Science Foundation under grants DMS 8919074 and ACS 8958522. The authors would like to thank Dr. Ralph Moir and Dr. Lewis Glenn at Lawrence Livermore National Lab for provision of facilities, technical advice, and encouragement.

10. References

[1] J.A. Blink, W.J. Hogan, J. Hovingh, W.R. Meier, and J.H. Pitts. The High-Yield Lithium-Injection Fusion-Energy (HYLIFE) Reactor, Lawrence Livermore National Laboratory, UCRL-53559 (1983).
[2] R.W. Moir, HYLIFE-II Inertial Confinement Fusion Reactor design, Fusion Technol. 19 (1991) 617–623.
[3] L.A. Glenn, Divergent and impulsive cross-flow over packed columnar array, Nucl. Engrg. Des. 56 (1980) 429–437.
[4] P. Colella and H.M. Glaz, Efficient solution algorithms for the Riemann problem for real gases, J. of Computational Phys. 59 (1985) 264–289.
[5] S.K. Godunov, A.V. Zabrodyn, and G.P. Prokopov, USSR Comput. Math. Math. Phys. 1 (1961) 1187.
[6] R.J. Leveque, Numerical Methods for Conservation Laws, Lectures in Mathematics (Birkhäuser Verlag, 1990) pp. 203–205.
[7] R. Hillier and J.M. Graham, Numerical prediction of shockwave diffraction, in: Proc. of the 15th Int'l Symp. on Shock Waves and Shock Tubes (1985) 391–397.
[8] J.E. Bowman and B.F. Niblett, The passage of a plane shock wave through a wire gauze, Proc. of the Phys. Soc. 68 (1956) 1008–1022.
[9] R. Kawamura and H. Kawada, A study on the attenuation of shock wave due to obstacles in the passage, J. of Phys. Soc. of Japan 12 (1957) 1290–1298.
[10] J. Liu, P.F. Peterson and V.E. Schrock, Blast venting through blanket material in the HYLIFE ICF reactor, Fusion Technol. 21 (1992) 1514–1519.
[11] G. Strang, On the construction and comparison of difference schemes, SIAM J. on Num. Anal. 5 (1968) 506–517.
[12] B. van Leer, Towards the ultimate conservative difference scheme. II: Monotonicity and conservation combined in a second order scheme, J. of Computational Phys. 14 (1974) 361–370.
[13] P. Woodward and P. Colella, The numerical simulation of two-dimensional fluid flow with strong shocks, J. of Computational Phys. 54 (1984) 115–173.
[14] G.C. Carafano, Benet Weapons Lab., Tech Report ARLCD-TR-84029 (1984).
[15] H.M. Glaz, P. Colella, I.I. Glass, and R.L. Deschambault, A numerical study of oblique-shock wave reflections with experimental comparisons, Proc. of the Royal Society, London. A398 (1985) 119–140.